

REPLY to the

Second Review of:

Mercury's Subsolar Sodium Exosphere: An ab initio Calculation to

Interpret MASCS/UVVS Observations from MESSENGER

Diana Gamberino, Audrey Vorburger, and Peter Wurz

1. The response to the referee comments are adequate except for the discussion of scale height. Actually what the authors say is correct for the true anomaly angles they calculate. However, the data that they are using, which is from Cassidy et al. (2015), are at TAA angles between 65 and 70 degrees, where the radiation pressure is maximum. In this case the radiation pressure is 50% of gravitational pressure, and the scale height is reduced to 2/3 of the no radiation pressure value. Therefore the scale height for T=594 is 39 km and the scale height for 1200 K (appropriate for PSD) is 78 km. I believe that the fit to the data is actually shallower than what is shown in the Gamberino paper, and fits the 78 km scale height quite well. This was the conclusion of Cassidy et al. (2015) and is why Cassidy et al. conclude that the data are consistent with photon-stimulated desorption. Also note that the maximum radiation pressure is at 65° not 90° because of the combined influence of heliocentric distance and radial velocity caused by the ellipticity of the orbit. If the simulated scale height is 57 km as they state, then the scale height that would have been attained without radiation pressure would have been 85.5 km, consistent with a temperature of 875 K. This is too hot to be consistent with thermal vaporization.

Indeed, the radiation pressure acceleration is maximum for TAAs around 65°-70° and 290°-295° (see Illustration 1 taken from Smyth, 1986).

However, the derived tangent column density profile (that we use in our work) reported by Cassidy et al. (2015), corresponds to a TAA=202°, according to the JPL's HORIZONS Ephemeris^[3].

The TAA=158° that we derived is incorrect but has the same radiation pressure acceleration value because both TAAs correspond to points in the orbit with the same distance to the Sun. Therefore our results do not change but we have corrected this mistake in the manuscript. We explain in the following how we derived this angle.

The True Anomaly Angle, denoted by ν , is derived from the definition for the distance from the Sun to Mercury, r_{orb} , given by the basic elliptical relation^[1]:

$$r_{orb} = \frac{a(1-e^2)}{1+e\cos(\nu)} \quad (1)$$

therefore the TAA is equal to (in degrees):

$$\nu = \arccos \left[\frac{1}{e} \left(\frac{a(1-e^2)}{r_{orb}} - 1 \right) \right] \frac{180^\circ}{\pi} \quad (2)$$

where e is the eccentricity of Mercury (=0.20563), a is the semimajor-axis of Mercury's orbit (=0.387AU). The tangent column density profiles derived by Cassidy et al. (2015) correspond to the MESSENGER observations taken on 23.04.2012 (see Illustration 3). According to the Geocentric Ephemeris of Mercury^[2], on 23 April 2012 Mercury was at a distance to the Sun of $r_{orb}=0.458$ AU.

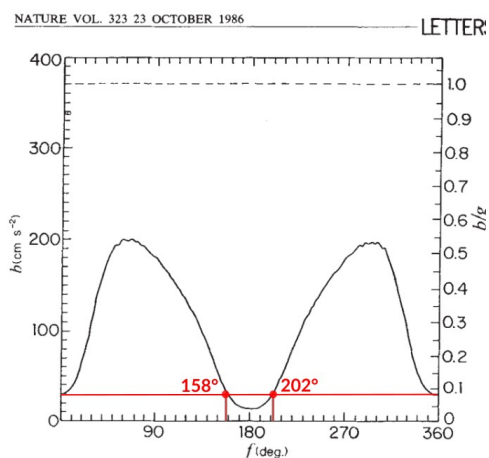


Fig. 1 Solar radiation pressure of sodium atoms near Mercury. The radiation acceleration (b) experienced by sodium atoms in Mercury's atmosphere because of resonance scattering in the solar D-lines is shown in absolute and surface gravity units as a function of the true anomaly angle f for the planet on its elliptical orbit around the Sun.

Illustration 1: Radiation Pressure Acceleration as a function of True Anomaly Angle (TAA) (Smyth, 1986).

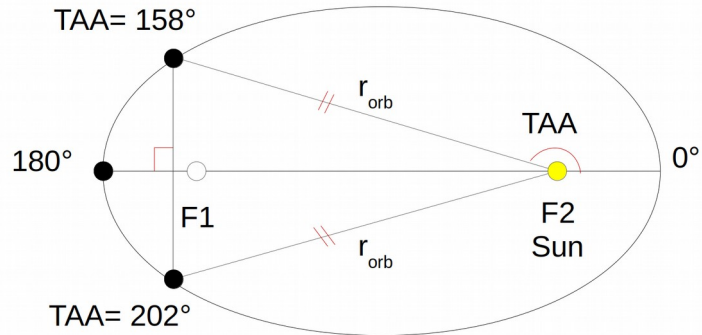


Illustration 2: Diagram of an ellipse illustrating the True Anomaly Angle. The angles 158° and 202° correspond to the same r_{orb} .

If we use these values: r_{orb} , e , and a in Eq. (2) we obtain: $v=158^\circ$. However, the cosine is an even-valued function, meaning that it is symmetric around π , therefore Eq. (2) has two solutions: $v_1=158^\circ$ and $v_2=202^\circ$. We used the JPLs HORIZONS System Ephemeris Tool^[3] and we found that the real TAA is actually 202° . Nevertheless, note that our results do not change because the radiation pressure acceleration has the same value for TAA= 158° and TAA= 202° , i.e., they correspond to the same r_{orb} (see Illustration 1 and 2).

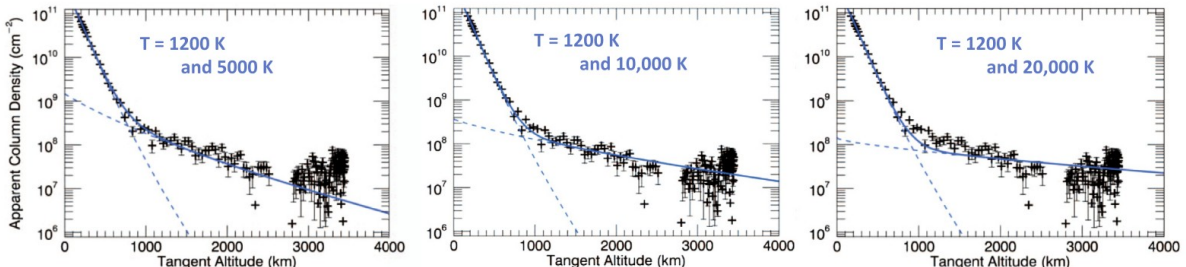


Fig. 7. Examples of fits including two temperature components. The individual components are shown by dashed blue lines, the sum of the two components by a solid blue line, and the data are represented by crosses. Unlike the cooler component of the exosphere, the hot component is well fit by a wide range of temperatures. In this example the hot component is equally well fit by 5000 K (left panel), 10,000 K (middle panel), and 20,000 K (right panel). For this reason we were unable to constrain the temperature of the hot component. The data were taken above the subsolar point on 23 April 2012. (For interpretation of the references to color in this figure legend, the reader is referred to the web version of this article.)

Illustration 3: Tangent column density profiles derived from MESSENGER observations during 23.04.2012 (see caption of Fig. 7 of Cassidy et al. (2015).)

Following Smyth (1986), we calculated that the radiation pressure acceleration is close to the minimum, for a TAA equal to 202° , and it is approximately equal to 28 cm s^{-1} (see Illustration 1). This is the value we use in our calculations.

Based on this radiation pressure acceleration we get a scale height for the thermal component of Na of 57 km for a surface temperature of 594 K.

References:

[1] Eq. (1) and (2) for the True anomaly angle (TAA) can be found in almost any book of Orbital Mechanics, <http://spiff.rit.edu/classes/phys440/lectures/ellipse/ellipse.html>

[2] $R_{\text{orb}}=0.458 \text{ AU} \rightarrow$ distance from Mercury to the Sun on **23.04.2012** taken from the Geocentric Ephemeris for Mercury: 2012 (<http://astropixels.com/ephemeris/planets/mercury2012.html>)

[3] JPLs HORIZONS System: <https://ssd.jpl.nasa.gov/horizons.cgi#results>

2. I still have additional questions about the results on thermal desorption.

In order to review the results in the Gamborino paper I asked the question, what is the thermal desorption rate at the subsolar point of Mercury?

These are my calculations:

1. The adsorption time is given by

$$\tau_{\text{ads}} = (1/v) \exp(Q/kT)$$

where $v = 10^{13} \text{ s}^{-1}$, $Q = 2 \text{ eV}$, $T = 594 \text{ K}$.

An activation energy of 2 eV is way too high for a Na atom falling onto the rock surface and becoming physisorbed. Realistic energies are around 0.5 eV; 2 eV would be for a Na in a mineral compound, but it cannot be expected that a Na atom falling onto the rock forms a mineral in this process, it basically just freezes out on the surface. The vibration frequency « v » in the above calculation by the reviewer is just a generic value for zero-order estimates, not specific to a Na atom on a rock surface.

Then $\tau_{\text{ads}} = 10^{-13} \exp(3.2 \times 10^{-12} \text{ erg}/(1.38 \times 10^{-16} * 594))$

$$\tau_{\text{ads}} = 8.99 \times 10^3 \text{ sec}$$

The surface number density is given by $n_{\text{surf}} = (dn/dt) \tau_{\text{ads}}$

Assume that 1/3 of the upward impact vaporization flux is lost. Then the downward flux is 2/3 F_{up}

This is a coarse estimate, we use the return fluxes calculated within our model based on first principles.

The surface number density is then 2/3 $F_{\text{up}} * 9 \times 10^3$

$$n_{\text{surf}} = 8.4 \times 10^{10} \text{ Na cm}^{-2}$$

This is the adsorbed number density on the surface, not in the exosphere.

What is the thermal desorption rate, K_{des} ?

$$K_{\text{des}} = A_{\text{des}} \exp(-E_{\text{des}}/kT)$$

This formula is a coarse approximation of the sublimation or evaporation from a surface. For sublimation it is better to use established measurements, e.g. Lide, D. R.: CRC Handbook of Chemistry and Physics, 84th Edition. CRC Press. Boca Raton, Florida; Section 4, 2003.

$A =$ vibration frequency = 10^{13} s^{-1}

This value is an estimate, but there is no support that it is the correct value for Na adsorbed on a regolith surface.

$E = 0.8 - 2.35 \text{ eV}$

If $E=2$ eV then the desorption rate (per atom) is $K_{des} = 1.1 \times 10^{-4} \text{ s}^{-1}$

The value of 2 eV corresponds to a strong binding of Na within a crystallographic compound. Usually, this value is used for sputtering of Na. Adsorbed Na, that has fallen back to the surface, will have a lower binding energy, since it is only physisorbed. Exploring the range of binding energies given above gives

$$E_{des} = 0.8 \text{ eV} \rightarrow K_{des} = 1.6 \times 10^{+6} \text{ s}^{-1}$$

$$E_{des} = 2 \text{ eV} \rightarrow K_{des} = 1.1 \times 10^{-4} \text{ s}^{-1}$$

$$E_{des} = 2.35 \text{ eV} \rightarrow K_{des} = 1.1 \times 10^{-7} \text{ s}^{-1}$$

With $E_{des} = 0.8$ eV the likely values for adsorbed Na on a surface, perhaps with even lower energy.

The thermal desorption rate is then:

$$\Phi_{therm} = n_{surf} * K_{des} = 9.3 \times 10^6 \text{ cm}^{-2} \text{ s}^{-1}$$

$$E_{des} = 0.8 \text{ eV} \rightarrow K_{des} = 1.6 \times 10^{+6} \text{ s}^{-1} \rightarrow \Phi_{therm} = 1.4 \times 10^{17} \text{ cm}^{-2} \text{ s}^{-1}$$

$$E_{des} = 2 \text{ eV} \rightarrow K_{des} = 1.1 \times 10^{-4} \text{ s}^{-1} \rightarrow \Phi_{therm} = 9.3 \times 10^6 \text{ cm}^{-2} \text{ s}^{-1}$$

$$E_{des} = 2.35 \text{ eV} \rightarrow K_{des} = 1.1 \times 10^{-7} \text{ s}^{-1} \rightarrow \Phi_{therm} = 9.5 \times 10^3 \text{ cm}^{-2} \text{ s}^{-1}$$

Given that E_{des} is not very constrained in its value, and a value of 0.8 eV or lower would be much more appropriate, the estimate by the reviewer of K_{des} is rather low, and a value for the desorbed flux of $\Phi_{therm} = 1.4 \times 10^{17} \text{ cm}^{-2} \text{ s}^{-1}$ is more likely.

This means that the thermal desorption rate is equal to the impact vaporization rate. It turns out that this is independent of the adsorption time.

Based on the arguments above, we disagree, and thermal desorption is a very fast process at these temperatures.

The ratio of the scale heights is

$$H_{IV} / H_{therm} = 6.7$$

We have calculated that the scale height for TD is 57 km and for MIV is 431 km (values derived from our numerical simulations), giving a ratio of $H_{MIV}/H_{TD} = 7.56$, pretty close to the ones of the reviewer, considering that we use a different TAA (see above).

the ratio of the number densities is

$$n_{0therm} / n_{0IV} = 2.6$$

If the fluxes are the same, the surface density in the exosphere at the surface has to be in the ratio of the square root of the temperatures (i.e. outward velocity). That means that there are 2.6 times as many thermal atoms at the surface than IV atoms but the scale height of the thermal atoms is 0.15 that of the IV atoms. The thermal atoms would not be seen.

The thermal Na are seen at low altitudes, below ~ 500 km. There, the observed scaled height in data reported by Cassidy et al. 2015 matches our calculation exactly, both for the MC model and for the theoretical model using the Chamberlain theory, for thermal desorption from a surface at 594 K.

3. Compare Figure 4 from Gamborino et al. with the above calculation. If the surface number density ratio of thermal to IV is 2.6 what would be the ratio of surface tangent columns? The tangent column is proportional to the surface number density and the square root of the scale height. The ratio of the surface number densities is 2.6, and the square root of the ratios of the scale heights is 0.385, so that the product is exactly 1.00. That means that the surface tangent columns of the thermal sodium and the IV are the same. The thermal component would not be seen in this case. It is curious that the same result is obtained independently of the adsorption energy because the number density at the surface is inversely related to the desorption rate, limiting the thermal component. The thermal to hot surface tangent columns in Gamborino et al. Figure 4 shows a ratio of about 250. If the adsorbed atoms are derived from the primary source (section 3.3) (e.g. Impact vaporization) then this cannot be the case. Other possibilities are that the PSD source partially thermalizes on impact with the surface (I think that Smyth came to this conclusion a long time ago.) But the other conclusion (from statement 1 above) is that the scale height of the cold component is more consistent with PSD, not thermal desorption.

We calculate the scale heights for TD, MIC, and PSD from the density profiles, which result from first principles calculations, with all the details given in the manuscript. The resulting numbers are given in Table 2. From the radial density profiles we calculate the profiles for the tangential column densities. These data are given in Figure 4, and the agreement between our calculations and the observations is fine.

We agree with the referee that Na atoms falling back to the surface will thermalize upon impact on the surface, perhaps only after a few impacts. This is true for Na released by PSD, MIC, and SP.

4. Page 13: The number density (in the exosphere) at the surface given on Gamborino line 29 is the same as I estimated for the adsorbed surface number density (which is not the same thing).

The referee gives an adsorbed surface density as $n_{surf} = 8.4 \times 10^{10}$ Na cm⁻², e.g. the number of Na atoms residing at the surface. The surface density we give in Table 2 is the number density in the exosphere at the surface. We agree with the referee that these two quantities are different.

5. It is not possible to understand the ratios of column densities in Table 2. I derived that the ratio of surface exospheric number density of thermal to IV is 2.6. The ratio of thermal to IV scale height is about 0.13, which we both agree. Therefore the ratio of the thermal column to IV column should be 0.34. Given that, the IV column would be 2×10^{10} cm⁻², or two orders of magnitude less than that given in table 2, column 3.

As detailed above, we disagree with the calculation of the thermal densities by the referee. However, we do want to stress that we calculate the release of Na for each release process from first principles. MIV release is calculated from the flux of impacting micro-meteorites. Thermal release is calculated from the evaporation of the ambient Na population on the surface, which is limited by the amount of available ambient Na. These processes are related to each other in that the returning Na feeds the ambient Na population at the surface.

6. The other questions I have are that the column abundance given for PSD in Table 2 is greater than the maximum possible for a collisionless exosphere, and that given for SP is larger than the observed abundance. These serious questions that need to be addressed because Mercury has an exosphere, not an atmosphere.

We calculate the scale height for PSD as $h_{PSD} = 232e3$ m (see Table 2).

The mean-free path at the surface for the PSD contribution can be estimated as

$$\Lambda = 1 / (n * \sigma) = 1 / (3.45e10 \text{ m}^{-3} * 1e-19 \text{ m}^2) \approx 2.9e8 \text{ m}$$

Thus, $h_{PSD} \ll \Lambda$, and we are still well in the collisionless regime at the surface, and above.

Moreover, we do mention that the values for PSD are upper limits, because of the competition between TD and PSD for the ambient Na population, which is strongly in favour for TD at these temperatures. Likely, the PSD contribution is actually much smaller, we estimate by a factor > 2500 . The same applies for SP, which we conclude is not relevant for the given observation parameters, i.e., observations near the sub-solar point which is shielded from the solar wind plasma. Our results show that PSD and SP for the observed parameters can not physically explain the properties of the exosphere observed, therefore we conclude that these processes are not dominant. Note that in our conclusions we mention that only TD and MIV are the best candidates to explain the observed column density profiles. No fitting was performed during our analysis.

Rosemary Killen

Referee

Mercury's Subsolar Sodium Exosphere: An *ab initio* Calculation to Interpret MASCS/UVVS Observations from MESSENGER

Diana Gamberino¹, Audrey Vorburger¹, and Peter Wurz¹

¹Space Research and Planetary Sciences, Physics Institute, University of Bern, 3012 Bern, Switzerland.

Correspondence: Diana Gamberino(gamberino@space.unibe.ch)

Abstract. The optical spectroscopy measurements of sodium in Mercury's exosphere near the subsolar point by MESSENGER MASCS/UVVS have been interpreted before with a model employing two exospheric components of different temperatures. Here we use an updated version of the Monte Carlo (MC) exosphere model developed by *Wurz and Lammer* (2003) to calculate the Na content of the exosphere for the observation conditions *ab initio*. In addition, we compare our results to the ones 5 according to Chamberlain theory. Studying several release mechanisms, we find that close to the surface thermal desorption dominates driven by a surface temperature of 594 K, whereas at higher altitudes micro-meteorite impact vaporization prevails with a characteristic energy of 0.34 eV. From the surface up to 500 km the MC model results agree with the Chamberlain model, and both agree well with the observations. At higher altitudes, the MC model using micro-meteorite impact vaporization 10 explains the observation well. We find that the combination of thermal desorption and micro-meteorite impact vaporization reproduces the observation of the selected day quantitatively over the entire observed altitude range, with the calculations performed based on the prevailing environment and orbit parameters. These findings help to improve our understanding of the physical conditions at Mercury's exosphere, as well as to better interpret mass-spectrometry data obtained to date and in future missions, such as BepiColombo.

1 Introduction

15 The Hermean particle environment is a complex system consisting of a surface-bounded exosphere (i.e., a collisionless atmosphere down to the planet's surface), and a magnetosphere that contains volatile and refractory species from the regolith as well as backscattered solar wind and interplanetary dust (*Killen et al.*, 2007). By the end of the 1970's Mariner 10 made the first observations of the composition of the exosphere around Mercury and found hydrogen and helium (*Broadfoot et al.*, 1976). **It was only during the year 1985, and further on, that many ground-based observations identified the presence 20 of sodium in the Hermean exosphere, and found that Na emissions are temporally and spatially variable (e.g., *Potter et al. (2007); Leblanc and Johnson (2010)*), often enhanced near north and south poles, have a moderate north-south asymmetry (e.g., *Potter and Morgan (1985); Sprague et al. (1998); Schleicher et al. (2004)*, are concentrated on the dayside (*Killen et al., 2007; Mouawad et al., 2011*), and are correlated with in situ magnetic field observations (*Mangano et al., 2015*).** Subsequent in situ observations made by MESSENGER provided a close-up look at the Hermean exosphere for over 25 10 Mercury years, including observations of the sodium exosphere. **These in situ observations show, in contrast with some**

5 **ground-based observations, that sodium has little or no year-to-year variation (Cassidy et al., 2015), and separately show a dawn-dusk asymmetry (Cassidy et al., 2016).** Due to the significant solar radiation pressure on the Na atoms in the exosphere, which can be up to half of Mercury's surface gravitational acceleration (Smyth, 1986; Ip, 1986), the sodium exosphere exhibits many interesting effects including the formation of an extended Na corona and a Na tail-like structure (Potter et al., 2007; Wang and Ip, 2011; Schmidt, 2013), observed also by MESSENGER (McClintock et al., 2008).

Hitherto several processes have been suggested to contribute to the sodium exosphere: thermal desorption/evaporation (TD), photon-stimulated desorption (PSD), solar wind sputtering (SP) and micro-meteorite impact vaporization (MIV) (e.g. McGrath et al. (1986); Hunten et al. (1988); Potter and Morgan (1997); Madey et al. (1998); Yakshinskiy and Madey (1999); Leblanc et al. (2003); Wurz and Lammer (2003); Killen et al. (2007)). For several decades the community has been debating on the 10 relative contribution of these mechanisms into the Hermean exosphere, and some modeling suggests that no single source mechanism dominates during the entire Mercury year (Sarantos et al., 2009; Leblanc and Johnson, 2010), and release mechanisms can influence each other (Mura et al., 2009). Laboratory experiments on lunar silicates simulants indicate that, under conditions such that thermal desorption is negligible (e.g., at high latitudes or at the lunar surface, where temperatures are below the sublimation point of sodium), much of the ambient sodium population on the surface is efficiently desorbed via 15 PSD (Yakshinskiy and Madey, 2000).

An extensive study of a subset of observations made by the Mercury Atmospheric and Surface Composition Spectrometer (MASCS) Ultraviolet and Visible Spectrometer (UVVS), on MESSENGER, was reported by Cassidy et al. (2015). From the measured Na emission in the exosphere, they derived the transversal column densities (TCD) profiles, which we use in this paper's analysis. Using the Chamberlain model they interpreted the observed TCDs with two thermal components: at low 20 altitudes, a thermal component of 1,200 K - which they suggest is due to PSD, and a hotter component at 5000 K - which they associate to MIV.

In contrast, we investigate all possible explanations using a different method. We use a Monte Carlo model in which we use different energy distributions for the particles released from the surface according to their release mechanism. Then we calculate the exospheric particle population by describing the motion of particles under the effect of a gravitational potential 25 and the radiation pressure from the Sun. We find that the Na observation can be explained by two combined processes: a low-energy process, TD, that dominates at low altitudes and is driven by the high surface temperature, and a comparably high-energy process, MIV, that is responsible for the Na observed at high altitudes.

We also implemented the Chamberlain model to compare directly to the Cassidy et al. (2015) results, as well as to compare them with our MC results. The main purpose of this comparison is to examine the implications and limits of the different 30 models in interpreting observations.

This paper is structured as follows: in Section 2 we briefly describe the previously published UVVS/MASCS observations of Na TCD that we use in this work. In Section 3 we describe the Chamberlain model, our MC model, and the modeled release processes. The resulting density profiles and a discussion of the limitations of the models are presented in Section 5, followed by a summary and conclusions in Section 6.

2 Observations

In this work we use the derived data reported by *Cassidy et al.* (2015), specifically the line-of-sight column density shown in Figure 7 in their work. They derived these data from MESSENGER MASCS/UVVS observations of the Na D1 and D2 lines taken above the subsolar point on 23 April, 2012. They do so by converting the UVVS emission radiance to line-of-sight 5 column density $N[\text{cm}^{-2}]$ using the formula $N = 10^9 4\pi I/g$, where $4\pi I$ is the radiance in kR and g is the rate at which sodium atoms scatter solar photons in the D1 and D2 lines.

Cassidy et al. (2015) analyzed the UVVS limb scan data by fitting the Chamberlain model (*Chamberlain*, 1963) to estimate the temperature and density of the near-surface exosphere, including the effects of radiation acceleration and photon scattering. The authors concluded that none or little evidence of thermal desorption of sodium was found. This finding was surprising and 10 was attributed to a higher binding energy of the weathered surface that would suppress thermal desorption. They also reported that observations show spatial and temporal variation but almost no year-to-year variation, and they do not observe the episodic variability reported by ground-based observers (**e.g., *Massetti et al.* (2017)**).

We chose these data because the observation geometry of MESSENGER MASCS/UVVS during that day, as illustrated in Fig. 2, is easy to understand and to reproduce by our model. The goal of this work is to show an interpretation from first 15 principles of the observed line-of-sight column density of a simple case observation with a model that accounts for several release processes rather than rely solely on the Chamberlain model that accounts only for thermal release.

3 Monte Carlo model description

We use an updated version of the MC model developed by *Wurz and Lammer* (2003). This model represents the exosphere by a large number of model particles, typically of the order of 10^6 . We calculate the orbits of each model particle given an initial 20 energy and angle selected randomly from a previously specified Maxwellian velocity distribution function for model particles released via TD and MIV, and non-Maxwellian ones for model particles released via PSD and SP (*Gamborino and Wurz* (2018); *Wurz and Lammer* (2003); *Vorburger et al.* (2015)). Because the gas is in a non-collisional regime we can simulate independently each release mechanism. Then we calculate each model particle trajectory under the effect of a gravitational potential, the effect of radiation pressure from the Sun, and using the local physical conditions. In this sense, our calculation is 25 “*ab initio*” because all the model parameters are derived from the observation conditions or physical principles.

The particle trajectory is determined for discrete altitude steps with start point at the surface until the particle either falls back to the surface, gets ionized somewhere on its path and thus is lost from the neutral exosphere, or leaves Mercury’s gravity field thus leaving calculation domain (which is given by the Hill radius). After simulating all model particles’ trajectories, we compute the species’ density and column density profiles as a function of altitude and tangent altitude by applying the 30 boundary conditions given from the particle release mechanism. For the calculation of the tangent altitude integration we assume a radially symmetric exosphere (see Figure 2). We also calculate the flux of particles released from the surface for each release process from the physical conditions of the release processes.

The number density of Na at the surface, or the surface atomic fraction, is only used for simulating the source population produced by the high-energy processes, which are MIV and SP. To simulate the ambient Na population, which is produced by TD and PSD, we use the number density resulting from the returning flux by MIV and SP.

We include the latest value for the atomic fraction of sodium in the surface derived from MESSENGER observations 5 (*Peplowski et al.*, 2015), as well as the effect of radiation pressure on Na atoms the same way as implemented by *Bishop and Chamberlain* (1989).

In the following we briefly describe the release and loss mechanisms, we explain the different assumptions concerning the Na on the surface that are important for the simulation and provide information about the model implementation.

3.1 Overview of release and loss processes

10 Up to now, various mechanisms have been proposed to be responsible for the input and loss of atomic species to and from planetary exospheres (*Wurz and Lammer*, 2003; *Killen et al.*, 2007; *Wurz et al.*, 2007). Here we describe TD, solar SP, PSD, and MIV.

15 Each release mechanism is described by a probability energy and angle distribution function that defines an ensemble of particles with a characteristic energy from which we determine the released flux from the surface. Here we provide a brief description of the release and loss mechanisms, the mathematical expressions for the different probability distribution functions we assume, characteristic energy, and release flux to be used in following sections.

3.1.1 Thermal desorption

To simulate TD we consider a Maxwellian distribution function with a characteristic energy given by the thermal energy, $E = k_B T_S$, where k_B is the Boltzmann constant and T_S is the temperature of the surface. The thermal speed of particles with 20 mass m released via TD is given by the mean speed of the ensemble: $v_{\text{the}} = \langle v \rangle = \sqrt{\frac{8k_B T_S}{\pi m}}$.

In theory, the released flux, Φ_{TD} , is proportional to the integral in the speed domain of the Maxwell-Boltzmann distribution. In this work, however, we consider that the released Na flux by TD is originated from a separate population. This flux is calculated as a contribution from the returning flux computed for MIV and SP mechanisms after running the simulation, and from the diffusion-limited exospheric flux calculated by *Killen et al.* (2004). This is further explained in detail in Sections 3.3 25 and 5.1.

3.1.2 Micro-meteorite impact vaporization

We determine the contribution to the exosphere by MIV in the same fashion as done by *Wurz et al.* (2010). First, we assume that Mercury's mass accretion rate for its apocentre and pericentre is, respectively, 10.7–23.0 tons/day (**Müller et al., 2002**). Similarly, *Cintala* (1992) reported that the meteoritic infall on Mercury is $1.402 \times 10^{-16} \text{ g cm}^{-2} \text{s}^{-1}$ for meteorites with mass of 30 $< 0.1 \text{ g}$, which corresponds to a particle radius of $< 0.02 \text{ m}$. This corresponds to a flux of 0.221 kg/s or 18.2 tons/day integrated over Mercury's surface. In contrast, *Borin et al.* (2009) reported an infall of $2.382 \times 10^{-14} \text{ g cm}^{-2} \text{s}^{-1}$, i.e., corresponding to

1540 tons/day, which is a factor 80 times higher compared to the value by Müller *et al.* (2002). Later on and using a different model, **Borin *et al.* (2010) reported an infall of $8.982 \times 10^{-15} \text{ g cm}^{-2} \text{s}^{-1}$, which is roughly 2.6 times smaller than their previous value.**

5 To calculate the exospheric densities and height profiles we derive the volatilization of surface material from the mass influx calculated before. For our simulation of particles released via MIV we considered an average temperature of 4000 K of the impact plume (value obtained from the range given by Eichhorn (1978a)). For the total number of released sodium atoms we find, accordingly, a mean MIV released flux of $2.45 \times 10^{11} \text{ m}^{-2} \text{s}^{-1}$ for $R_{\text{orb}} = 0.458 \text{ AU}$, which corresponds to the observation day. We consider a uniform MIV flux over the whole planet.

3.1.3 Sputtering

10 This process refers to the impact of solar wind ions onto the surface causing the release of volatiles and refractory elements mostly near the cusp regions. The predicted value of solar wind flux to the surface near the southern cusp is four times larger than in the north because of the offset of Mercury's magnetic dipole of $0.2 R_M$ ($\sim 400 \text{ km}$) northward from the planetary center (Anderson *et al.*, 2011). **The plasma pressures in the cusp are 40% higher when the Interplanetary Magnetic Field (IMF) is anti-sunward than when it is sunward (Winslow *et al.*, 2012), indicating that the effect of the IMF B_x direction**

15 **is present. At the subsolar point, the surface is shielded from the solar wind by Mercury's magnetosphere (see review by Raines *et al.* (2014)).** However, there is a small neutral component of the solar wind (NSW), of about 10^{-5} – 10^{-3} particles at IAU (Collier *et al.*, 2003), which is not deflected by the Hermean magnetic field, thus permanently contributing to sputtering on the entire dayside of the planet. The energy distribution adapted with an energy cut-off (Wurz and Lammer, 2003) given by the binary collision limit of particles sputtered from a solid, $f(E_e)$, with energy E_e of the sputtered particle, has been given as:

20

$$f(E_e) = C \frac{E_e}{(E_e + E_b)^3} \left\{ 1 - \left[\frac{(E_e + E_b)}{E_{\max}} \right]^{1/2} \right\}, \quad (1)$$

where C is the constant of normalisation, E_b is the surface binding energy of the sputtered particle which we consider equal to 2.0 eV for Na, taken from SRIM (Ziegler *et al.*, 2010), and where E_{\max} is the maximal energy that can be transferred in a binary collision. The maximum of the energy distribution is at $E_{\max} = E_b/2$. This mechanism will release all species from the 25 surface into space, reproducing more or less the local surface composition on an atomic level. The total sputtered flux from the surface, Φ_i , of species i is:

$$\Phi_i = \Phi_{\text{SW}} \cdot Y_i = N_i(0) \langle v_i \rangle, \quad (2)$$

where Φ_{SW} is the solar wind flux impinging on the surface, Y_i is the total sputter yield for species i . From Eq. 2 we get $N_i(0)$, the exospheric density at the surface, with $\langle v_i \rangle$ the mean speed of sputtered particles. For the simulation we considered the 30 mean values of particle flux and solar wind speed at Mercury for a solar wind dynamic pressure $P_{\text{dyn}} = 20 \text{ nPa}$ determined by Massetti *et al.* (2003): $\Phi_{\text{sw}} = 4.1 \times 10^{12} \text{ m}^{-2} \text{s}^{-1}$ and $v_{\text{sw}} = 440 \text{ km/s}$.

3.1.4 Photon-Stimulated Desorption (PSD)

When a surface is bombarded by photons of sufficient energy it can lead to the desorption of neutral atoms or ions. Solar photons with energy ≥ 5 eV ($\leq \lambda = 2500$ Å) have enough energy to release atomic sodium from the surface of regolith grains (Yakshinskiy and Madey, 1999). In particular, the experimental results by Yakshinskiy and Madey (2000, 2004) on lunar samples show that released neutral Na atoms by Electron-Stimulated Desorption (ESD) and PSD have supra-thermal speeds. Since then, several energy and velocity distributions have been used to describe particles released via PSD, varying between Maxwellian (e.g., Leblanc *et al.* (2003)) to non-Maxwell distributions (e.g., Schmidt (2013)). However, the use of a non-Maxwellian distribution, in particular the Weibull distribution, has recently proven to be most suitable to describe this release mechanism (Gamborino and Wurz, 2018). The normalized Weibull distribution allows for a wide range of shapes using only two parameters for its definition. For PSD, this function is expressed as follows:

$$f(v, v_0, \kappa) = \kappa \Gamma\left(1 + \frac{1}{\kappa}\right) \left(\frac{m}{3k_B T_s}\right)^{1/2} \left[(v - v_0) \sqrt{\frac{m}{3k_B T_s}} \Gamma\left(1 + \frac{1}{\kappa}\right) \right]^{\kappa-1} \times \exp\left[-\left((v - v_0) \sqrt{\frac{m}{3k_B T_s}} \Gamma\left(1 + \frac{1}{\kappa}\right)\right)^\kappa\right] \quad (3)$$

where k_B is the Boltzmann constant, m is the mass of the species, T_s is the surface temperature, Γ is the Gamma function, v_0 is the offset speed, and κ is the shape parameter of the distribution. The parameters have been derived as $\kappa = 1.7$ and speed offset of $v_0 = 575$ m/s by Gamborino and Wurz (2018).

3.2 Loss processes

We include the following exospheric loss processes: (1) gravitational escape, (2) surface adsorption, and (3) ionization. The escape speed from Mercury's surface is $v_{\text{esc}} = 4.3$ km/s, which is small enough to allow the escape of many exospheric particles, particularly the light ones. We compute the fraction of atoms lost by photo-ionization at each time step in the trajectory calculation, and we use the typical photo-ionization rates of Na at Mercury, which are 7.2×10^{-6} s $^{-1}$ and 7.9×10^{-6} s $^{-1}$ during low and high Solar activity, respectively (<http://phidrates.space.swri.edu/>). On average, it takes a few hours until a sodium atom is ionized, which gives enough time to complete an exospheric trajectory for most released particles. Sodium atoms will go back to Mercury's surface and be adsorbed, unless they are lost due to ionization or escape Mercury's gravity.

In Figure 1 we show the different energy spectra for Na from the probability distribution functions, each normalized to a maximum of one, for the four release mechanisms. Atoms released via TD have an energy distribution dependent on the local surface temperature, which is represented by the *solid-black* curve, corresponding to a characteristic energy of 0.06 eV and a temperature of 594 K. Atoms released via this process have a relatively low characteristic energy compared to the escape energy of sodium atoms from Mercury's surface, which is 2.07 eV for Na atoms. Thus, TD leads to a near-surface Na exosphere that does not contribute to the planetary loss. On the other hand, atoms released via SP (*dashed* curve), have significantly higher characteristic energy (1 eV) and a distribution skewed to higher energies (see Eq. 1), thus reaching higher altitudes and contributing to the planetary loss. **At the subsolar point, ion fluxes onto the surface and consequently the**

sputter yields are low compared to the pole regions (where the magnetic field cusps are located), therefore sputtered atoms can only form a low-density exosphere (Wurz *et al.*, 2010). A long-tailed positively skewed distribution also describes the energy distribution for PSD release (see Eq. 3) shown as the *dashed-dotted* curve in Fig. 1, which has a characteristic energy of ~ 0.1 eV, thus particles can reach higher altitudes compared to those released via TD. As can be seen in the plot, 5 the energies are mostly below escape. Finally, atoms released via MIV (*dotted* curve) are modeled by a thermal distribution with temperatures of 4000 K, thus higher characteristic energy (0.34 eV) compared to the regular TD. **MIV contributes to the exosphere in a comparable amount like SP (Wurz *et al.*, 2010), if solar wind sputtering is active. Unfortunately, the micro-meteorite influx onto Mercury's surface is not known very accurately, as discussed above.**

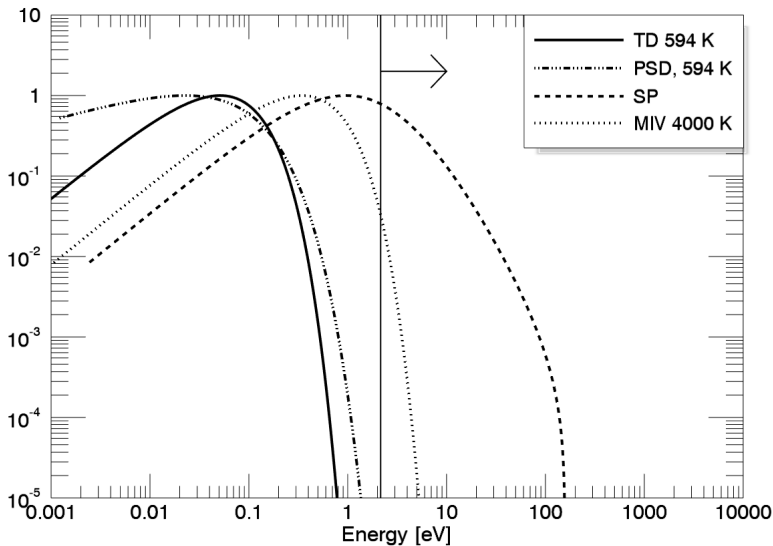


Figure 1. Normalized energy distribution functions for several release mechanisms active on Mercury's surface to produce the sodium exosphere. The vertical solid line marks the value at which sodium atoms have enough energy to escape the gravitational field of Mercury.

3.3 Sodium in and at the Surface

10 *Smyth and Marconi* (1995) introduced a qualitative description of the fate of sodium atoms ejected in Mercury's environment using two populations, the “source” and the “ambient” atoms. A few years later, *Morgan and Killen* (1997) expanded the description to include the diffusion of sodium from inside the regolith to the surface and the description of the expanding vapor cloud after the impact of micrometeorites. Here we consider these two populations; a first population, the so-called “source atoms”, which are atoms chemically-bonded in the minerals on the surface and are released by high-energy processes, either 15 by MIV or SP. The source atoms are predominantly ionically bonded to the oxygen in a bulk silicate (*Madey et al.*, 1998) with binding energy larger than 0.5 eV.

The released Na atoms may either escape, or fall back on the surface and become ambient particles after few impacts on the surface (measured in experiments by *Yakshinskiy and Madey* (1999, 2000, 2004)). These particles are thermally accommodated

to the local surface temperature and have counterparts absorbed in the regolith with a binding energy less than 0.5 eV, according to *Hunten et al.* (1988). We model this population by low energy processes such as TD and PSD. An illustration depicting the different release, returning, and loss fluxes is shown and explained in Section 5.1.

4 Model implementation

5 The MC model, as described above, and the Chamberlain model (as described in the Appendix A) are evaluated for the parameters of the MESSENGER observation conditions as listed in Table 1. In this section we describe in detail how we obtained these parameters.

Table 1. Parameters for simulation.

Orbital and geographical parameters	All processes
Orbital radius (R_{orb} [AU])	0.458
True Anomaly Angle (TAA)	202 [◊] †
Solar Zenith Angle (SZA)	0° ††
Longitude	0°
Physical parameters	
Number of model particles	10^6
Surface temperature [K]	594
Surface Na atomic fraction	0.0234*
Global meteoritic infall	10.52 tons/day**
UV flux at surface ϕ_{ph} [$\text{m}^{-2}\text{s}^{-1}$]	$1.57 \times 10^{20} \diamond$
Radiation acceleration (b_{rad} [cm s^{-2}])‡	28

†TAA taken from JPL's HORIZONS Ephemeris (<https://ssd.jpl.nasa.gov/horizons.cgi>).

††Latitude=0°.

* Intermediate Composition (*Peplowski et al.*, 2015).

** calculated for the specific $R_{\text{orb}} = 0.458$ AU, and TAA= 202[◊] from the range given by *Müller et al.* (2002) which depends on the orbital distance.

◊ for PSD.

‡*Smyth and Marconi* (1995).

4.1 Simulation parameters and geometry

To reproduce the measured TCD profile reported by *Cassidy et al.* (2015), we have to know some input values for the simulation parameters. Using SPICE and Mercury's ephemeris data we find the corresponding parameters for the time of the MESSENGER observations (listed in Table 1). The dayside limb-scans were taken when Mercury had a TAA= 202[◊]; MESSENGER was near the apogee, and with the UVVS line-of-sight pointing approximately northward - as shown in the illustration in Figure 2; see also top of Figure 2 in *Cassidy et al.* (2015). During the day of the observation MESSENGER

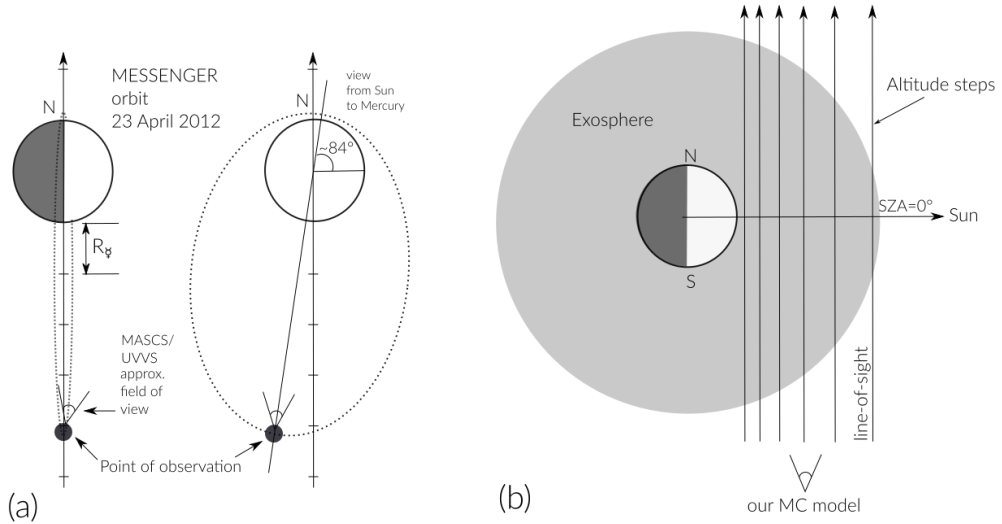


Figure 2. (a) Representation to scale of MESSENGER's orbit around Mercury during the time of observations (orbits parameters taken from www.nasa.gov). (b) Scheme of the line-of-sight used in the simulations (distance between altitude steps is not to scale). *Solid-black* lines on (b) represent the altitude steps for integration of the the column density when SZA=0°.

made three orbits around Mercury with an orientation such that its orbit plane was almost perpendicular with respect to the light rays coming from the Sun, as represented in the illustration in Figure 2 (mind that this is just a simplified representation of the real situation). Each altitude profile extends from just above the surface, as low as 10 km, to several thousand kilometers above the surface.

Given the position of the spacecraft with respect to Mercury and the direction of the UVVS line-of-sight during the time of observation, we simulate particles ejected at latitude= 0°, SZA= 0°, and calculated the contribution to the TCD from this position. This is the closest to the real observation geometry that our model can compute.

In Figure 2.(a) we illustrate the orbit geometry and position of the MESSENGER spacecraft during the time of observation. In Figure 2.(b) we also illustrate the orientation of the tangent (to the surface) altitude steps we used in our model for the integration of the column density. The dawn/dusk asymmetry is not considered because the time of the observation does not include these regions.

The sodium surface atomic fraction, indicated in Table 1, is used to calculate the surface number density and release flux, and it is used only for calculating the source population produced by the high-energy processes, which are MIV and SP. To simulate the ambient sodium population, which is produced by TD and PSD, we use the surface number density resulting from the returning flux to the surface by MIV and SP.

On the other hand, the radiation pressure depends on the true anomaly angle and the solar zenith angle, and we use the value for radiation acceleration taken from *Smyth and Marconi (1995)* for the given TAA during the time of observations. We assume

the same orbital and physical parameters for our implementation of the Chamberlain model modified by adding radiation pressure.

After computing the density profiles we integrate along the line-of-sight for different altitude steps and for SZA=0° to obtain the limb scans as a function of tangent altitude.

5 4.1.1 Temperature model

According to the infrared measurements made on Mariner 10 (*Chase et al.*, 1976), which only include observations from the night-side up to 8:00 LT on the dayside, and considering Mercury as a blackbody emission radiator, the extrapolated dayside surface temperature as a function of latitude ϕ and longitude θ must follow a “1/4”-law with illumination angle, and decrease like “ $1/r^2$ ” where r is the distance of Mercury to the Sun. Neglecting the thermal inertia of Mercury’s lithosphere, the local 10 dayside surface temperature for $0 < |\theta| < \pi/2$ can be written as:

$$T_s(\phi, \theta) = T_{min} + (T_{max} - T_{min})(\cos \phi \cos \theta)^{1/4}$$

where T_{max} is the effective temperature at the subsolar point, T_{min} is the night-side temperature, the longitude θ is measured from the planet-Sun axis, and the latitude ϕ is measured from the planetary equator. To determine the effective temperature at subsolar point we used the blackbody Stefan-Boltzman law to obtain:

$$15 \quad T_{\text{eff}} \approx T_{\text{Sun}} \left[\left(\frac{R_{\text{Sun}}}{R_{\text{orb}}} \right)^2 \frac{1 - \alpha}{\epsilon} \right]^{1/4} \quad (4)$$

where T_{eff} is the effective temperature of the surface, R_{orb} is the distance to the Sun, R_{Sun} is the solar radius, $T_{\text{Sun}} = 5778$ K is the effective solar temperature, $\alpha = 0.07$ is the albedo (*Balogh et al.*, 2000) and $\epsilon = 0.9$ is the emissivity (*Murcray et al.*, 1970; *Saari and Shorthill*, 1972; *Hale and Hapke*, 2002). During the day of observations Mercury was at a distance of $R_{\text{orb}} = 0.458$ AU to the Sun. Using this value and the temperature formula from above (Eq. 4), we calculated a surface temperature of 20 $T_{\text{eff}} = T_S = 594$ K at the subsolar point. This is the temperature we used for the TD and PSD calculations.

In Figure 3 we show an example of the tangent column density profiles computed for the different release mechanisms and with different characteristic temperatures. All processes were simulated with and without radiation pressure to compare them. We fixed all profiles at altitude zero and a tangent column density normalized to one to show the different shapes and slopes for the different mechanisms and different physical parameters specified in the legend.

25 5 Results and Discussion

Using the parameters listed in Table 1, we simulate sodium atoms released via TD, PSD, MIV, and SP and calculated the exospheric density profiles up to 10^5 km. The integral along the line-of-sight gives us the column density and if we choose the tangent altitude we also obtain the TCD as a function of altitude. The surface TCD and released flux obtained from the simulation for each mechanism are listed in Table 2. Independently, we also implemented the Chamberlain model in the same 30 fashion as *Cassidy et al.* (2015) did to compare it to our results (see description in Appendix A).

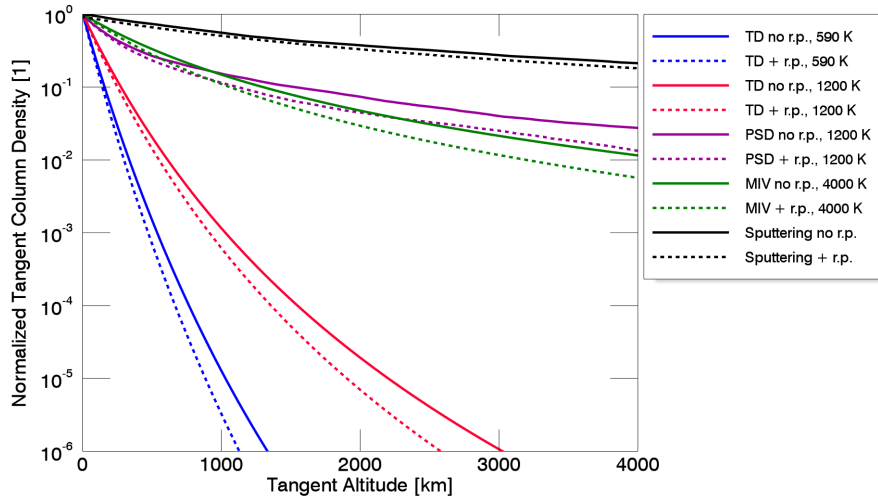


Figure 3. Column density profiles as a function of tangent altitude for Na where the column density at the surface is normalized to one, and for the different release mechanisms: TD, PSD, MIV, and SP with and without radiation pressure (r.p.) centered at subsolar point and for different surface temperature values. The simulation was done with an ensemble of 10^6 particles, and Mercury at a $TAA=202^\circ$ and $R_{orb} = 0.458$ AU.

Figure 4 includes two plots where we show the derived MESSENGER observations (black cross marks) together with the results from our MC simulations, and the results using the Chamberlain model. On the left figure, we plot the sodium TCD as a function of altitude for: TD (dashed-black curve), MIV (dashed-grey curves), SP (dash-dot-dot-grey curve), and PSD (vertical-dash black curve). The results using the Chamberlain model with the modification 5 for radiation pressure are also plotted: the curve with square symbols corresponds to a surface temperature of 594 K, and the curve with circle symbols corresponds to an assumed temperature of 2500 K, with the TCD at the surface of this component adjusted to match the observations. The sum of the two Chamberlain profiles are represented by the solid-light-grey curve. On the right figure, we only plot our MC results for TD with $T = 594$ K, and MIV (multiplied by a factor of 0.5) for $T = [3000, 4000, 5000]$ K, together with the derived MESSENGER observations. We would like to 10 point out again, that no fitting to any surface density was applied in our model. Rather, the surface density is a result from the model itself.

At low altitudes the Chamberlain model and the TD simulation for the surface temperature agree very well, and both also agree reasonably well with the observations, which is expected from a Maxwellian population thermalized with the surface. Note that the calculated thermal profiles, both with the Chamberlain model and with our MC model, are based on the surface 15 temperature, which was derived separately from the orbit position of Mercury and were not fitted to the data. The release fluxes for TD and PSD are both calculated from the ambient sodium population atoms, which we derived in the next section. The fall off above 1000 km of the TD 594 K curve is a result of the loss of neutral sodium atoms due to ionization. Compared to any other mechanism modeled here, TD is the best match to the observations at low altitudes.

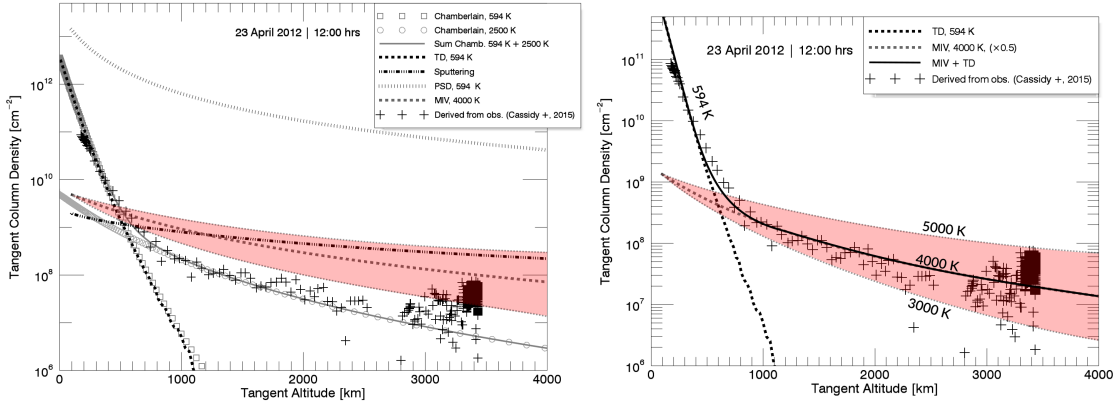


Figure 4. Left: Plots of the derived TCD from observations (black crosses), of the results from our calculations with no correction factors, and of the results using the Chamberlain model. The resulting TCD profiles from our MC model are plotted as follows: TD is the *dashed-black* curve, MIV between 3000 K and 5000 K is the shaded red area, the *dashed-grey* curve is MIV with a mean temperature of 4000 K, SP is the *dash-dot-dot-dot* grey curve, and PSD is the *vertical-dash* curve. The resulting profiles using the Chamberlain model are represented as the *square-* and *circle-symbols* curves. The sum of the two Chamberlain profiles represented by the *solid-light-grey* curve. Right: Plots of the derived TCD from observations (black crosses), and of the results from our calculations: the *dashed-black* curve for TD, the results for MIV between 3000 K and 5000 K is the shaded red area, the *dashed-grey* curve is MIV with a mean temperature of 4000 K. MIV curves were multiplied by 1/2. The sum of TD and MIV profiles is shown as the *solid-black* curve.

At altitudes above ~ 600 km the Chamberlain model for 594 K shows too low densities and only a high-temperature component of 2500 K fits the data, similar to *Cassidy et al. (2015)*. The SP curve is too flat and does not match the observations at any given altitude. As described further on, and as shown in Figure 6, the sputtered component of the tangent column density is expected to be substantial mainly at high latitudes, but the observation geometry gives preference to mechanisms happening at low latitudes, around the subsolar point.

The limitation of Chamberlain theory (*Chamberlain, 1963*) in this context is that it was originally developed for Earth's exosphere where the only controlling factors considered are the gravitational attraction and the "*thermal energy conducted from below*" (also known as exobase). For the case of Mercury, the only layer below the exosphere is the surface. Meaning that, the only "source" mechanism of exospheric particles considered in Chamberlain model is what we consider in our MC model as Thermal Desorption.

Using the Chamberlain theory implies that the only way to increase the particles' characteristic energy (and thus able to reach high altitudes) is by increasing the surface temperature. One way to do this is by micrometeorite impacts, which can lead to a Maxwellian exospheric population with a temperature of the order of a few thousand Kelvin, which can explain the high-energy component in the observations. Another way to increase the temperarure is by heating the surface with solar radiation. But as calculated, the surface temperature of Mercury at the subsolar point and at $TAA = 202^\circ$ is 594 K. This temperature is not enough to let particles reach high altitudes, much higher temperatures are needed as shown in Figure 4. Consequently, the Chamberlain model works fine only for an exospheric population that is in thermal equilibrium with the surface temperature. For other non-Maxwellian and more energetic populations, the Chamberlain model is inadequate.

Hence, it is inevitable to consider other, non-thermal and more energetic, release processes to explain the Na exosphere at higher altitudes. Our results show that PSD and MIV are two possible non-thermal and high-energy mechanisms that can explain the observations at high altitudes, as shown in Figure 4. Our MC model of the MIV TCD profile gives a good match with the observed data at high altitudes with a temperature of $4000\text{ K} \pm 1000\text{ K}$, a temperature that is consistent with *Eichhorn* 5 (1978a) laboratory data. An even better match is reached by adjusting the surface column density by only a factor of 0.5. On the other hand, the PSD TCD profile does not fit quite as well to the observations and it has to be scaled with a factor of 4×10^{-4} to match part of the tail, which will be addressed below.

Since TD is competing with PSD for the ambient Na atoms on the surface, the Na available for PSD is much less, or none available at all, in the extreme case (as explained below). Therefore, the plotted curve of PSD is just an upper limit. The TCD 10 profile for SP is also plotted in Figure 4 for precipitating ion fluxes of the cusp region. Since the observations are at the subsolar point, the surface is shielded from precipitating ions (*Kallio and Janhunen*, 2003), and the SP contribution to the exosphere for these observations has to be considered as an upper limit as well. Moreover, the TCD from SP falls off much less with altitude than the observations.

5.1 Source and loss fluxes

15 Director, Space Science and Planetology The sodium loss from the exosphere has to be supplied by Na from the surface to sustain a stable exosphere over several Mercury years as it was observed (*Cassidy et al.*, 2015). As mentioned in Section 3.3, the source population of Na to the exosphere is considered to come mainly from the release via SP and MIV. The fraction of this population that comes back to the surface will become the ambient population and be available for TD and PSD. The conservation of mass allows us to quantify the amount of Na in the ambient population at the subsolar point, which is available 20 for TD, by considering that the sum of the Na diffused from regolith to the surface plus the return fluxes from MIV and SP has to be equal the loss due to TD. Mathematically, the latter is stated as:

$$\Phi_{\text{source}}^{\text{Ambient}} = \Phi_{\text{Diff.}} + \Phi_{\text{return}}^{\text{MIV}} + \Phi_{\text{return}}^{\text{SP}} \quad (5)$$

$$\Phi_{\text{loss}}^{\text{Ambient}} = \Phi_{\text{release}}^{\text{TD}} \cdot \chi_{\text{Tot}}^{\text{TD}} \quad (6)$$

25 where χ is the total fraction of Na loss, which includes the losses by ionization and gravitational escape. $\Phi_{\text{Diff.}}$ is the diffusion-limited exospheric flux calculated by *Killen et al.* (2004) to be $< 10^7\text{ cm}^{-2}\text{ s}^{-1}$. Note that the fluxes' subscripts *source* and *loss* are calculated just for the ambient population and does not represent the global flux. For a steady state system:

$$\Phi_{\text{source}}^{\text{Ambient}} - \Phi_{\text{loss}}^{\text{Ambient}} = 0 \quad (7)$$

Combining Equations 5, 6, and 7 we derive $\Phi_{\text{release}}^{\text{TD}}$ as follows:

$$30 \quad \Phi_{\text{release}}^{\text{TD}} = \frac{\Phi_{\text{Diff.}} + \Phi_{\text{return}}^{\text{MIV}} + \Phi_{\text{return}}^{\text{SP}}}{\chi_{\text{Tot}}^{\text{TD}}} = \frac{1.0 \times 10^7\text{ cm}^{-2}\text{ s}^{-1} + (5.4 \times 10^5 + 3.28 \times 10^5)\text{ cm}^{-2}\text{ s}^{-1}}{0.0102} = 1.06 \times 10^9\text{ cm}^{-2}\text{ s}^{-1} \quad (8)$$

From Eq. 8 we can derive the surface density, as $n_0 = \frac{\Phi_{\text{release}}^{TD}}{v_{\text{th}}} = 1.44 \times 10^{10} \text{ m}^{-3}$, where $v_{\text{the}} = \sqrt{8k_B T/\pi m} = 739 \text{ m/s}$.

The radial column density, NC , can be approximated as: $NC \approx n_0 \cdot H = 8.21 \times 10^{14} \text{ m}^{-2} = 8.21 \times 10^{10} \text{ cm}^{-2}$. The rest of the results of our simulations, together with the derived quantities for the ambient population are shown in Table 2.

Table 2. Results from the MC simulation.

Property	TD	MIV	PSD	SP
Scale height [km]	57	431	232	748
Surface density (n_0 [m^{-3}]) [‡]	1.44×10^{10}	5.97×10^6	3.45×10^{10}	3.72×10^6
Column density (NC [cm^{-2}])	8.21×10^{10}	2.57×10^{12}	8.0×10^{15}	2.79×10^{12}
Total released Na flux [$\text{cm}^{-2} \text{ s}^{-1}$]	1.06×10^9	5.74×10^5	3.63×10^9 *	1.32×10^6
Total fraction of lost particles [†]	0.0102	0.0589	0.0307	0.7510

[‡]Based on Na surface fraction from Intermediate Composition (Peplowski *et al.*, 2015), and used for MIV, PSD, and SP.

* Adjusted to observations by a multiplication factor of 4×10^{-4} , and is considered an upper limit.

[†]Including the losses by gravitational escape and ionization.

Figure 5 is a scheme illustrating the Na release processes and fate due to the different release mechanisms. For the given observations, we calculated the Na release flux from the surface and determined the losses for each process. The fraction of Na that is not lost returns to the surface and becomes part of the ambient population available for TD and PSD.

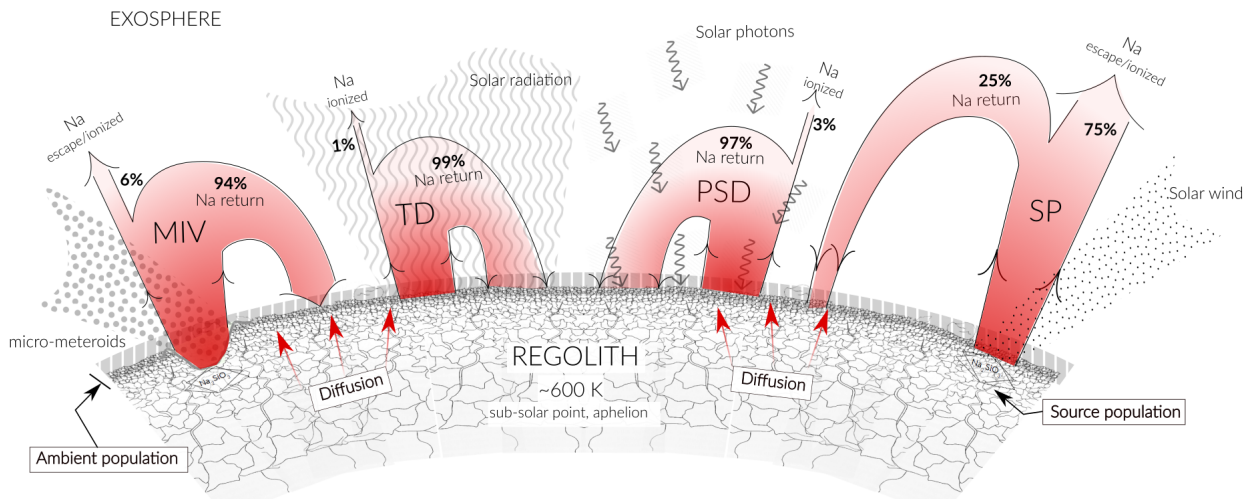
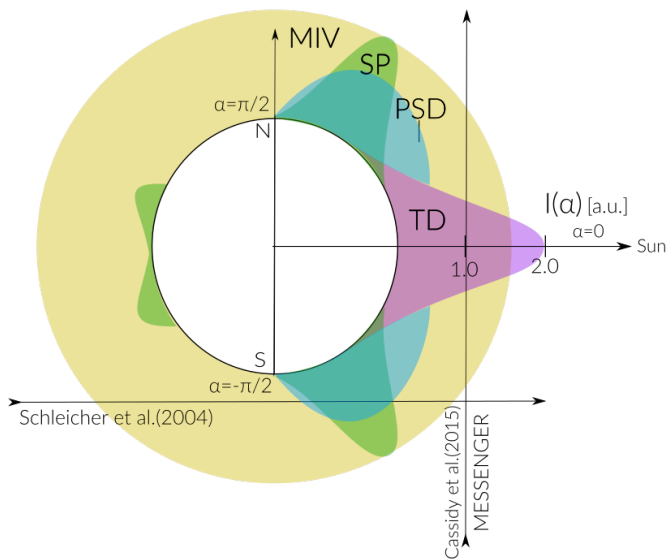


Figure 5. Scheme illustrating the different released fluxes of Na due to the different release mechanisms from the mineral compound (the source population) and from surface (the ambient population). The illustration is not to scale.

Figure 6 is an illustration of the spatial distribution of the derived released Na fluxes as a function of solar zenith angle. The radial scale represents the magnitude difference of the release flux “intensity”, $I(\alpha)$, for the different release mechanisms (the units are arbitrary). Note that this diagram does not represent the spatial distribution of Na depending on the mechanism, but just the magnitude of the release flux for each mechanism. At the subsolar point, the main contribution of Na to the

exosphere is TD with a release flux of two orders of magnitude higher compared to the other release processes, and with an exponential decay towards the poles because of the strong temperature dependence of sublimation. The solar wind sputtering on the surface acts mainly at high latitudes ($\alpha \approx \pm\pi/2$), and is also a strong function of latitude decay. We consider that MIV acts uniformly on the entire planet, thus the release flux is not angle dependent. PSD has a cosine dependence with SZA, but 5 since it competes with TD it is most important at mid- to high latitudes.

This illustration shows the main release mechanisms given a certain line-of-sight observation geometry. For instance, the ground based observations done by *Schleicher et al.* (2004) during Mercury's transit had a limb line-of-sight similar to the horizontal line shown in Figure 6. **The main contribution for those limb observations when $\alpha \approx \pm\pi/2$, include a sum of SP and PSD, which provides a sputter high-energy Na exosphere and a low-energy photo-desorbed ambient Na** 10 **population, which was already discussed by *Mura et al.* (2009).** On the other hand, the vertical line-of-sight path crossing TD and MIV represents the line-of-sight of the approximate direction of MESSENGER's field of view during observations on 23 April 2012 (*Cassidy et al.*, 2015) and discussed here. **If observations are made with a line-of-sight corresponding to $\alpha \approx \pm\pi/4$ for instance, the analysis of the source mechanisms becomes complicated because all release mechanisms will be active in some extent, and thus it will be difficult to differentiate them.**



26

Figure 6. Scheme of the intensity distributions for the different release mechanisms as a function of solar zenith angle. The units are arbitrary but orders of magnitude are taken from the results of our model. The horizontal arrow is an example of the line-of-sight of the ground-based observations by *Schleicher et al.* (2004). Vertical arrow represents the approximate direction of MESSENGER's field of view during observations on 23 April 2012 (*Cassidy et al.*, 2015).

5.2 Is there a permanent Na atom layer on the surface?

Reviewed earlier reports (e.g. *Leblanc et al.* (2003)) conclude there is a non-uniform spatially distributed but permanent “reservoir” of atomic Na available on the surface, forming part of the ambient population. This reservoir is not strongly chemically bounded to the mineral grains, but it is physisorbed on the surface and being on the surface it is also not part of

5 the exosphere. Let us consider sodium adsorbed in an atomic state on the surface rather than chemically bounded to the crystal structure in the regolith (consistent with laboratory experiments by *Yakshinskiy and Madey* (2000, 2004)). We can calculate the theoretical Na gas density above the surface and the evaporated flux by using the empirical equation for the Na vapor pressure (*Lide*, 2003) and considering a surface temperature of $T = 594$ K at subsolar point, this gives a sodium vapor pressure of $P_0 = 7.44$ Pa.

10 The corresponding theoretical evaporated flux of sodium atoms from this surface reservoir would be 6.71×10^{21} atoms per $\text{cm}^2 \text{ s}$. This value is 14 orders of magnitude higher than the thermal Na release flux we derived from measurements, which is 4.34×10^8 atoms per $\text{cm}^2 \text{ s}$. Even if the atomic Na is bound to the surface with a higher binding energy, the sublimation flux will still be enormous at this temperature. Thus, it is clear that the TD flux is limited by the availability of ambient Na on the 15 surface, and given the large difference in theoretical and derived release fluxes, all the ambient Na is in the exosphere and not on the surface near the subsolar point. This implies that all the ambient sodium released from the bulk or that has fallen back onto the surface near the subsolar point will be immediately evaporated to the exosphere leaving no atomic Na left in areas near the subsolar point. Therefore, based on these considerations, PSD can not compete to desorb sodium because there is no Na left available on the surface.

These interpretations follow the line of what was previously deduced from experiments by *Madey et al.* (1998) carried 20 out with various oxide surfaces that resembled the hermean and lunar regolith. The authors found that at temperatures in the range of $\sim 400\text{--}800$ K, TD of fractional Na monolayers occurs even for low alkali coverages, with the desorption barrier (and surface lifetimes) increasing on a radiation damaged surface. Specially, their measurements indicate that at equatorial regions TD rapidly depletes the alkali atoms from the surface reservoir, whereas it is less efficient at high latitudes. This is consistent 25 to our finding that at low altitudes and at the subsolar point, TD is the dominant process and is responsible for the exospheric Na at low altitudes up to about 600 km. On the other hand, MIV is a very plausible mechanism to explain the high-energy component, since it releases Na present in the bulk, and thus is not limited by the availability of Na on the surface.

6 Conclusions

We present the results of our Monte Carlo model of the hermean sodium exosphere and compare them with the sodium tangent column density profile derived from MASCS/UVVS measurements during the day 23 April 2012 (*Cassidy et al.*, 2015). Using 30 the correct parameters for TAA and T_S for the day of the observations, we calculate the density profiles of sodium atoms ejected from Mercury’s surface through TD, PSD, MIV, and SP as release mechanisms.

We reproduce the derived sodium TCD profile as a function of altitude: below 500 km release via TD dominates, governed by a surface temperature of 594 K corresponding to a characteristic energy of 0.06 eV. Because of the very high release fluxes,

the Na in the exosphere near the surface is due to TD, limited by the supply of available Na atoms on the surface. Only at higher altitudes the contribution by MIV prevails up to the observed 4000 km with a characteristic energy of 0.34 eV.

For the first 500 km with the MC model TD results agree well Chamberlain model using a local surface temperature of 594 K, and both agree with the measurements. As we go further away from Mercury's surface though, there is a more energetic 5 component of Na atoms in the exosphere which we find to be the result of MIV.

We have also shown that if there would be an ambient sodium layer available on the surface at the subsolar point, this would have to be immediately evaporated due to the high volatility of Na at such a high surface temperature at the given observation time. The Na release by TD is strongly limited by the supply of free Na to the surface at the local surface temperature. Moreover, release by PSD can only be responsible for the Na exosphere population at higher altitudes, because of the higher energies of 10 the released Na atoms. However, we find that we can only give an upper limit for the release of Na via PSD for the investigated observations.

Our results diverge substantially from the results by *Cassidy et al.* (2015). While their work is elucidating and explains the derived observations in terms of two thermal release populations using the Chamberlain model, it seems they arrive at a confounding near-to-the-surface sodium temperature of 1,200 K. Using their assumptions and the Chamberlain model we get 15 good agreement of our model (MC and Chamberlain) for the calculated surface temperature, which is half their value, and the results using our MC model confirms the same number.

As mentioned before, our results apply to the specific observation conditions we discussed. As shown in our diagram in Figure 6, for other observation geometries, i.e., a different line of sight and TAA, other surface release mechanisms might be active and can dominate over others. Future work will include a larger data set with different observation 20 conditions to test our model and determine the influence of other release processes.

The use of mass spectrometers is crucial to study the surface composition of Mercury and ultimately to understand the origin of species found in the exosphere since they come from the regolith and crust (except for the noble gases, hydrogen and a few volatile species such as sulphur, which are abundant in the micro-meteorite population). To prepare for the SERENA investigation (*Orsini et al.*, 2010), to be performed on board of ESA's BepiColombo planetary orbiter (*Milillo et al.*, 2010), we 25 have updated and extended our MC model, originally developed by *Wurz and Lammer* (2003), which is a tool to quantitatively predict exospheric densities for several release processes using the actual physical parameters of the release process.

Acknowledgements. We gratefully thank the Swiss National Science Foundation (200020–172488) for supporting this work. The first author also wants to thank André Galli for his support and help while writing this paper. We also thank the Linux Cluster UBELIX team for letting us use their cluster to run our simulations.

Appendix A: Chamberlain Model Implementation

Chamberlain's model (Chamberlain, 1963) is based on Liouville's Theorem applied to a collisionless exosphere where the gravitational attraction and the thermal energy conducted from below are the controlling factors. The Liouville equation is solved using a Maxwellian distribution as the boundary condition at the exobase. The velocity distribution is then integrated 5 in the region allowed by the trajectory in a gravitational field and over the velocity space, which can be divided into different populations that represent different types of particle orbits: *ballistic* (captive particles whose orbits intersect the critical level, i.e., surface in Mercury's case), *satellite* (captive particles orbiting above the critical level), and *escaping* (particle's velocity is larger than the escape velocity). This leads to analytic expressions for the density distributions and the loss flux. The number density at a given altitude r is given by:

$$10 \quad n(r) = n(r_c) \exp[-(\lambda_c - \lambda)] \zeta(\lambda) \quad (A1)$$

where the parameter λ represents the absolute value of the potential energy expressed in units of $k_B T_c$ as follows:

$$\lambda_c(r) = \frac{GMm}{k_B T_c r} = \frac{v_{esc}^2}{V^2} \quad (A2)$$

where $v_{esc} = (2GM/r_c)^{1/2}$ is the escape velocity and $V = (2k_B T_c/m)^{1/2}$ is the most probable Maxwellian velocity (thermal velocity), G is the gravitational constant, M is the mass of the planet, m is the mass of the species, k_B the Boltzmann constant, 15 T_c the exobase temperature, and r the radial distance from the center of the planet. The sub-index c stands for *critical level* that corresponds to the exobase, which corresponds to Mercury's surface in this case.

Equation A1 is a combination of the barometric density equation with a partition function $\zeta(\lambda)$, where $n(r_c)$ is the density at the critical level. The factor ζ may be regarded as the fraction of the isotropic Maxwellian distribution that is present at a given altitude, subject to conservation of energy and angular momentum. For no dynamical restrictions to the orbit, $\zeta = 1$, which 20 leads to the generalized form of the (isothermal) barometric law. However, at substantial distances above the critical level the barometric law breaks down because the pressure at large distances is decidedly directional and the mean kinetic energy per atom decreases. The atmosphere is not strictly in hydrostatic equilibrium, moreover it is expanding slightly, i.e., some matter is being lost, which in the kinetic theory corresponds to evaporative loss. To treat the density distribution accurately it is necessary to examine the individual particle orbits which is the case when $\zeta \neq 0$. The analytical expressions of ζ for each class 25 of particle orbits can be found in Chamberlain (1963). The effect of radiation pressure on sodium atoms was also incorporated following Bishop and Chamberlain (1989). Examples of sodium column density profiles for the different types of trajectories are displayed in Fig. A1 considering a surface temperature of $T_c = 594$ K.

On the other hand, sodium atoms in the atmosphere of Mercury can be accelerated by solar radiation pressure resulting from resonant scattering of solar photons. In earlier works it has been suggested that radiation pressure could sweep sodium off the 30 planet, provided that the sodium is non-thermal [e.g. Ip (1986); Bishop and Chamberlain (1989); Wang and Ip (2011)]. Under the influence of radiation pressure, particles' trajectories can depart significantly from Keplerian counterparts, thus modifying the exosphere structure. As a consequence, the sodium atoms might be expected to be pushed away from the Sun towards the

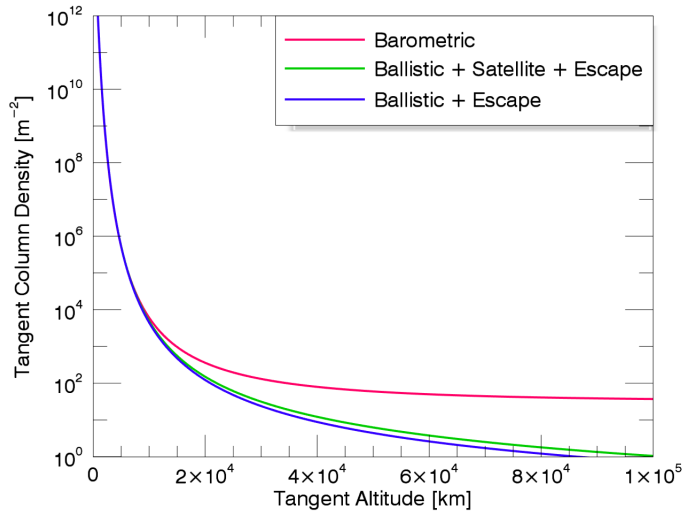


Figure A1. Examples of the TCD profiles for sodium for an exobase temperature of 594 K using the Chamberlain model. The pink curve represents the density profile for the barometric law, the green curve represents a combination of ballistic + satellite + escape orbits, and the blue curve represents density profiles including ballistic + escaping particles.

night-side of Mercury as the radiation pressure increases. It has been shown that for sodium atoms, radiation acceleration can be up to 54% of the surface gravity (*Smyth and Marconi*, 1995). We follow *Bishop and Chamberlain* (1989) by modifying the potential energy function, $|\lambda(r)|$, and we implement the solar radiation acceleration expression as used by *Wang and Ip* (2011). Equation A3 is the new expression for the potential energy in units of $k_B T$ and is a combination of the acceleration by gravity and radiation forces:

$$\lambda(r) = \frac{GMm}{k_B T r} - \frac{mb_{rp}r \cos(\theta)}{k_B T} \quad (A3)$$

where b_{rp} is the radiation acceleration and is a function of TAA. We used the value of b_{rp} from *Smyth and Marconi* (1995) for $\text{TAA}=202^\circ$. θ is the solar zenith angle. Figure A2 is another example of sodium column density profiles considering different values of surface temperature, true anomaly angle (TAA) and solar zenith angle (SZA). The variation with TAA modifies substantially the density profiles. When the radiation pressure is maximal, i.e., $\text{TAA} \approx 65^\circ, 280^\circ$ and $\text{SZA}=0^\circ$ (subsolunar point), the density profiles have a steeper slope, which means that exospheric particles are pushed back towards the surface. On the other hand, when the radiation pressure is minimal but not zero (that is when $\text{SZA}=90^\circ$), i.e., $\text{TAA}=180^\circ, 180^\circ$ and $\text{SZA}=89^\circ$, the density profiles have a flatter slope, which means that exospheric particles are able to reach higher altitudes.

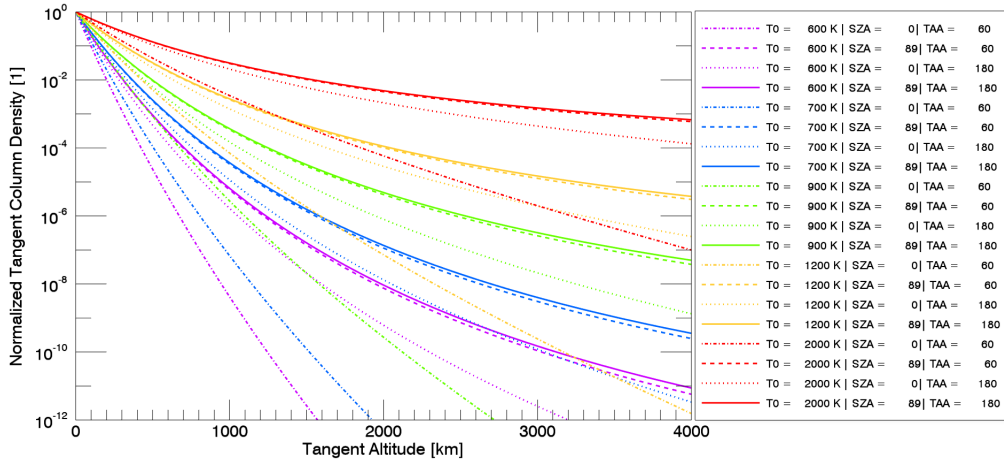


Figure A2. Examples of the TCD profiles for sodium using Chamberlain model for different values of temperature, $T_0 = [600, 700, 900, 1200, 2000]$ K, and fixing parameters for maximum and close to minimum radiation pressure (max: TAA $\approx 65^\circ$ and SZA = 0° , \sim min: TAA $\approx 180^\circ$ and SZA = 89°).

References

Anderson, B. J., Johnson, C. L., Korth, H., Purucker, M. E., Winslow, R. M., Slavin, J. A., Solomon, S. C., McNutt Jr., R. L., Raines, J. M., and Zurbuchen, T. H.: The global magnetic field of Mercury from MESSENGER orbital observations, *Science*, 333, 1859–1862, doi:10.1126/science.1211001, 2011.

5 Balogh, A., Bird, M., Blomberg, L., Bochsler, P., Bougeret, J. L., Brückner, J., Iess, L., Guest, J., Langevin, Y., Milani, A., Sauvad, J. A., Schmidt, W., Spohn, T., von Steiger, R., Thomas, N., Torkar, K., Wänke, H. and Wurz, P.: BepiColombo—An interdisciplinary cornerstone mission to the planet Mercury, *ESA-SCI(2000)1* Noordwijk, The Netherlands, European Space Agency, <http://solarsystem.estec.esa.nl/Mercury/MercuryAssess.htm>, 2000.

Bishop, J. and Chamberlain, J. W.: Radiation pressure dynamics in planetary exospheres: A “natural” framework, *Icarus* 81, 145–163, doi:10.1016/0019-1035(89)90131-0, 1989.

10 Borin, P., Cremonese, G., Marzari, F., Bruno, M., and Marchi, S.: Statistical analysis of micrometeorites flux on Mercury, *Astronomy and Astrophysics* Volume 503, Issue 1, 259–264. doi: 10.1051/0004-6361/200912080, 2009.

Borin, P., Bruno, M., Cremonese, G., Marzari, F. Estimate of the neutral atoms’ contribution to the Mercury exosphere caused by a new flux of micrometeoroids. *Astronomy and Astrophysics*, 517, A89. DOI: <https://doi.org/10.1051/0004-6361/201014312>. 2010.

15 Broadfoot, A. L., Shemansky, D. E., and Kumar, S.: Mariner 10 - Mercury atmosphere, *Geophysical Research Letters*, Vol. 3, p. 577–580. doi: 10.1029/GL003i010p00577, 1976.

Burger, M. H., Killen, R. M., Vervack Jr., R. J., Bradley, E. T., McClintock, W. E., Sarantos, M., Benna, M., and Mouawad, N.: Monte Carlo modeling of sodium in Mercury’s exosphere during the first two MESSENGER flybys, *Icarus* 209, 63–74. <http://dx.doi.org/10.1016/j.icarus.2010.05.007>, 2010.

20 Cassidy, T. A., Merkel, A. W., Burger, M. H., Sarantos, M., Killen, R. M., McClintock, W. E., and Vervack, R. J.: Mercury’s seasonal sodium exosphere: MESSENGER orbital observations, *Icarus*, Volume 248, 547–559. doi: 10.1016/j.icarus.2014.10.037, 2015.

Cassidy, T. A., McClintock, W. E., Killen, R. M., Sarantos, M., Merkel, A. W., Vervack, R. J., Burger, and Matthew, H.: A cold-pole enhancement in Mercury's sodium exosphere, *Geophysical Research Letters* 43-21 1944-8007. <http://dx.doi.org/10.1002/2016GL071071>, 2016.

Chamberlain, J. W.: Planetary coronae and atmospheric evaporation, *Planet. Space Sci.* 11, 901–960. [http://dx.doi.org/10.1016/0032-0633\(63\)90122-3](http://dx.doi.org/10.1016/0032-0633(63)90122-3), 1963.

Chase, S. C., Jr., Miner, E. D., Morrison, D., Muench, G., and Neugebauer, G.: Mariner 10 infrared radiometer results - Temperatures and thermal properties of the surface of Mercury, *Icarus*, Vol. 28, p. 565–578. doi: 10.1016/0019-1035(76)90130-5, 1976.

Cintala, M. J.: Impact-induced thermal effects in the lunar and Mercurian regoliths, *J. Geophys. Res.* 97, 947–973, <https://doi.org/10.1029/91JE02207>, 1992.

10 Collier, M. R., Moore, T. E., Ogilvie, K. W., Chornay, D. J., Keller, M. C., Fuselier, B. L., Quinn, J., Wurz, P., Wuest, P., Hsieh, K. C.: Dust in the wind: The dust geometric cross section at 1 AU based on neutral solar wind observations, *Solar Wind X, American Institute Physics* 679, 790-793. DOI: 10.1063/1.161871, 2003.

Eichhorn, G.: Heating and vaporization during hypervelocity particle impact, *Planet. Space Sci.*, 26, 463–467, [https://doi.org/10.1016/0032-0633\(78\)90067-3](https://doi.org/10.1016/0032-0633(78)90067-3), 1978a.

15 Gamborino, D. and Wurz, P.: Velocity distribution of Na released by photons from planetary surfaces, *Planet. Space Sci.*, 159, 97 – 104. <https://doi.org/10.1016/j.pss.2018.04.021>, 2018.

Hale, A.S. and Hapke, B.: A Time-Dependent Model of Radiative and Conductive Thermal Energy Transport in Planetary Regoliths with Applications to the Moon and Mercury, *Icarus*, Volume 156, Issue 2, 318-334, <https://doi.org/10.1006/icar.2001.6768>, 2002.

Hunten, D. M., Shemansky, D. E., and Morgan, T. H.: The Mercury atmosphere, *In: Vilas, F., Chapman, C.R., Matthews, M.S. (Eds.), Mercury*. University of Arizona Press, pp. 562–612, 1988.

20 Ip, W. H.: The sodium exosphere and magnetosphere of Mercury, *Geophys. Res. Lett.* 13, 423–426. <http://dx.doi.org/10.1029/GL013i005p00423>, 1986.

Johnson, R. E., Leblanc, F., Yakshinskiy, B. V., and Madey, T. E.: Energy distributions for desorption of sodium and potassium from ice: the Na/K ratio at Europa, *Icarus* 156, 136–142. <https://doi.org/10.1006/icar.2001.6763>, 2002.

25 Kallio, E. and Janhunen, P.: Solar wind and magnetospheric ion impact on Mercury's surface, *Geophysical Research Letters*, vol 30, no.17, 1877, doi:10.1029/2003GL017842, 2003.

Killen, R. M., Potter, A. E., and Morgan, T. H.: Spatial distribution of sodium vapor in the atmosphere of Mercury, *Icarus* (ISSN 0019-1035), vol. 85, p. 145–167. doi: 10.1016/0019-1035(90)90108-L., 1990.

30 Killen, R. M., Potter, A., Fitzsimmons, A., and Morgan, T. H.: Sodium D2 line profiles: clues to the temperature structure of Mercury's exosphere, *Planet. Space Sci.* 47, 1449–1458, doi: 10.1016/S0032-0633(99)00071-9, 1999.

Killen, R., G. Sarantos, M., Potter, A. E., and Reiff, P.: Source rates and ion recycling rates for Na and K in Mercury's atmosphere, *Icarus* 171, 1–19. doi:10.1016/j.icarus.2004.04.007, 2007.

35 Killen, R., Cremonese, G., Lammer, H., Orsini, S., Potter, A. E., Sprague, A. L., Wurz, P., Khodachenko, M., Lichtenegger, H. I. M., Milillo, A., and Mura, A.: Processes that promote and deplete the exosphere of Mercury, *Space Sci. Rev.* 132, 433–509. <http://dx.doi.org/10.1007/s11214-007-9232-0>, 2007.

Killen R., Shemansky, D., and Mouawad N.: Expected emission from Mercury's exospheric species, and their ultraviolet-visible signatures, *Astrophysical Journal Supplement*, 181 (2), pp. 351–359. doi:10.1088/0067-0049/181/2/351, 2009.

Leblanc, F., Delcourt, D., and Johnson, R. E.: Mercury's sodium exosphere: magnetospheric ion recycling, *J. Geophys. Res.* 108, No. E12, 5136, doi:10.1029/2003JE002151, 2003.

Leblanc, F. Doressoundiram, A., Schneider, N., Massetti, S., Wedlund, M., López, Ariste, A., Barbieri, C., Mangano, V., and Cremonese, G.: Short-term variations of Mercury's Na exosphere observed with very high spectral resolution, *Geophys. Res. Lett.* 36, L07201. 5 https://doi.org/10.1029/2009GL038089, 2009.

Leblanc, F. and Johnson, R. E.: Mercury exosphere I. Global circulation model of its sodium component, *Icarus*, Volume 209, Issue 2, 280-300, ISSN 0019-1035, https://doi.org/10.1016/j.icarus.2010.04.020, 2010.

Lide, D. R.: CRC Handbook of Chemistry and Physics, 84th Edition. *CRC Press. Boca Raton*, Florida; Section 4, 2003.

Madey, Theodore E., Yakshinskiy, B. V., Ageev, V. N., and Johnson, R. E.: Desorption of alkali atoms and ions from oxide surfaces - 10 Relevance to origins of Na and K in atmospheres of Mercury and the Moon, *Journal of Geophysical Research*, vol. 103, 5873–5887. doi: 10.1029/98JE00230, 1998.

Mangano, V., Massetti, S., Milillo, A., Plainaki, C., Orsini, S., Rispoli, R., Leblanc, F.: THEMIS Na exosphere observations of Mercury and their correlation with in-situ magnetic field measurements by MESSENGER, *Planetary and Space Science*, Volume 115, 102–109, https://doi.org/10.1016/j.pss.2015.04.001, 2015.

15 Massetti, S., Orsini, S., Milillo, A., Mura, A., DeAngelis, E., Lammer, H., and Wurz, P.: Mapping of the cusp plasma precipitation on the surface of Mercury, *Icarus* 166, 229–237. doi: 10.1016/j.icarus.2003.08.005, 2003.

Massetti, S., Mangano, V., Milillo, A., Mura, A., Orsini, S., Plainaki, C.: Short-term observations of double-peaked Na emission from Mercury's exosphere, *Geophys. Res. Lett.*, 44, 2970–2977, doi:10.1002/2017GL073090, 2017.

McClintock, W. E., Bradley, E. T., Vervack, R. J., Killen, R. M., Sprague, A. L., Izenberg, N. R., Solomon, S. C.: Mercury's Exosphere: 20 Observations During MESSENGER's First Mercury Flyby. *Science* 321, 92–94. DOI:10.1126/science.1159467, 2008.

McGrath, M. A., Johnson, R.E., and Lanzerotti, L.J.: Sputtering of sodium on the planet Mercury, *Nature* 323, 694–696. http://dx.doi.org/10.1038/323694a0, 1986.

Milillo, A., Fujimoto, M., Kallio, E., Kameda, S., Leblanc, F., Narita, Y., Cremonese, G., Laakso, H., Laurenza, M., Massetti, S., McKenna-Lawlor, S., Mura, A., Nakamura, R., Omura, Y., Rothery, D. A., Seki, K., Storini, M., Wurz, P., Baumjohann, W., Bunce, E., Kasaba, Y., 25 Helbert, J., and Sprague, A.: The BepiColombo mission: an outstanding tool for investigating the Hermean environment, *Planetary and Space Science* 58 40–60. doi:10.1016/j.pss.2008.06.005, 2010.

Morgan, T. H. and Killen, R. M: A non-stoichiometric model of the composition of the atmospheres of Mercury and the Moon, *Planetary and Space Science*, Volume 45, Issue 1, 81–94, ISSN 0032-0633, doi: 10.1016/S0032-0633(96)00099-2, 1997.

Mouawad, N., Burger, M. H., Killen, R. M., Potter, A. E., McClintock, W. E., Vervack, R. J., Bradley, E. T., Benna, M., Naidu, 30 S.: Constraints on Mercury's Na exosphere: Combined MESSENGER and ground-based data, *Icarus*, Volume 211, Issue 1, 21–36, https://doi.org/10.1016/j.icarus.2010.10.019, 2011.

Müller, M., Green, S. F., McBride, N., Koschny, D., Zarnecki, J. C., and Bentley, M. S.: Estimation of the dust flux near Mercury, *Planet. Space Sci.* 50, 1101–1115. https://doi.org/10.1016/S0032-0633(02)00048-X, 2002.

Mura, A., Wurz, P., Lichtenegger, H. I. M., Schleicher, H., Lammer, H., Delcourt, D., Milillo, A., Orsini, S., Massetti, S., and Khodachenko, 35 M. L.: The sodium exosphere of Mercury: Comparison between observations during Mercury's transit and model results, *Icarus* 200, 1–11. doi:10.1016/j.icarus.2008.11.014, 2009.

Murcray, F. H., Murcray, D. G. and Williamns, W. J.: Infrared emissivity of lunar surface features. I. Balloon-borne observations. *J. Geophys. Res.* 75, 2662-2669. https://doi.org/10.1029/JB075i014p02662, 1970.

Orsini, S., Livi, S., Torkar, K., Barabash, S., Milillo, A., Wurz, P., Di Lellis, A. M., Kallio, E. and The SERENA team: SERENA: A suite of four instruments (ELENA, STROFIO, PICAM, and MIPA) on board BepiColombo-MPO for particle detection in the Hermean environment, *Planet. Space Sci.* 58, 166–181. doi:10.1016/j.pss.2008.09.012, 2010.

Peplowski, P., Lawrence, D., Feldman, W., Goldsten, J., Bazell, D., Evans, L., Head, J., Nittler, L., Solomon, S., and Weider, S.: 5 Geochemical terranes of Mercury's northern hemisphere as revealed by MESSENGER neutron measurements, *Icarus* 253 346–363. <http://dx.doi.org/10.1016/j.icarus.2015.02.002>, 2015.

Potter, A. E. and Morgan, T. H.: Discovery of sodium in the atmosphere of Mercury, *Science* 229, 651–653. <http://dx.doi.org/10.1126/science.229.4714.651>, 1985.

Potter, A. E. and Morgan, T. H.: Variation of sodium on Mercury with solar radiation pressure, *Icarus* (ISSN 0019-1035), vol. 71, p. 472–477. 10 [https://doi.org/10.1016/0019-1035\(87\)90041-8](https://doi.org/10.1016/0019-1035(87)90041-8), 1987.

Potter, A. E. and Morgan, T. H.: Sodium and potassium atmospheres of Mercury, *Planetary and Space Science*, Volume 45, Issue 1, 95–100. doi: 10.1016/S0032-0633(96)00100-6, 1997.

Potter, A. E., Killen, R. M., and Morgan, T. H.: The sodium tail of Mercury, *Meteoritics and Planetary Science*, vol. 37, no. 9, pp. 1165–1172. doi: 10.1111/j.1945-5100.2002.tb00886.x, 2002.

Potter, A. E., Killen, R. M., and Sarantos, M.: Spatial distribution of sodium on Mercury, *Icarus*, 181, 1–12. 15 <http://dx.doi.org/10.1016/j.icarus.2005.10.026>, 2006.

Potter, A. E., Killen, R. M., and Morgan, T. H.: Solar radiation acceleration effects on Mercury sodium emission, *Icarus* 186 571–580. <https://doi.org/10.1016/j.icarus.2006.09.025>, 2007.

Raines, J. M., Gershman, D. J., Slavin, J. A., Zurbuchen, T. H., Korth, H., Anderson, B. J., Solomon, S. C.: Structure and dynamics 20 of Mercury's magnetospheric cusp: MESSENGER measurements of protons and planetary ions, *J. Geophys. Res. Space Physics*, 119, 6587–6602, doi:10.1002/2014JA020120, 2014.

Saari, J. M. and Shorthill, R. W.: The sunlit lunar surface. I. Albedo studies and full Moon temperature distribution, *The Moon* 5, 161–178. doi:10.1007/BF00562111, 1972.

Sarantos, M., Slavin, J. A., Benna, M., Boardsen, S. A., Killen, R. M., Schriver, D., Travnicek, P.: Sodium-ion pickup observed above the 25 magnetopause during MESSENGER's first Mercury flyby: Constraints on neutral exospheric models, *Geophys. Res. Lett.*, 36, L04106, doi:10.1029/2008GL036207, 2009.

Schleicher, H., Wiedemann, G., Wohl, H., Berkefeld, T., and Soltau, D.: Detection of neutral sodium above Mercury during the transit on 2003 May 7, *Astron. Astrophys.* 425, 1119–1124. <http://dx.doi.org/10.1051/0004-6361:20040477>, 2004.

Schmidt, C. A.: Monte Carlo modeling of north-south asymmetries in Mercury's sodium exosphere, *J. Geophys. Res. Space Physics* 118, 30 4564–4571. <https://doi.org/10.1002/jgra.50396>, 2013.

Shemansky, D.E.: Revised atomic species abundances at Mercury: the debacle of bad g values, *The Mercury Messenger*, 1, Issue 2, 1988.

Simpson, W. C., Wang, W. K., Yarmo, J. A., and Orlando, T. M.: Photon- and electron-stimulated desorption of O⁺ from zirconia, *Surface Science* 423 225–231. [https://doi.org/10.1016/S0039-6028\(98\)00908-X](https://doi.org/10.1016/S0039-6028(98)00908-X), 1999.

Smyth, W. H.: Nature and variability of Mercury's sodium atmosphere, *Nature* 323, 696–699. <http://dx.doi.org/10.1038/323696a0>, 1986.

Smyth, W. H. and Marconi, M. L.: Theoretical overview and modeling of the sodium and potassium atmosphere of Mercury, *Astrophysics Journal* 441, 839–864. doi:10.1086/175407, 1995.

Sprague, A. L., Schmitt, W.J., and Hill, R. E.: Mercury: Sodium atmospheric enhancements, radar-bright spots, and visible surface features, *Icarus* 136, 60–68. <http://dx.doi.org/10.1006/icar.1998.6009>, 1998.

Takakuwa, Y., Niwano, M., Nogawa, M., Katakura, H., Matsuyoshi, S., Ishida, H., Kato, H., and Miyamoto, M.: Photon-stimulated desorption of H⁺ ions from oxidized Si(111) surfaces, *The Japan Society of Applied Physics*, Part 1 <https://doi.org/JAPNDE28>, 2581, 1989.

Vervack, R. J., Killen, R. M., McClintock, W. E., Merkel, A. W., Burger, M. H., Cassidy, T. A., and Sarantos, M.: New discoveries from MESSENGER and insights into Mercury's exosphere, *Geophysical Research Letters* 43-22, 1944-8007.

5 http://dx.doi.org/10.1002/2016GL071284, 2016.

Vorburger, A., Wurz, P., Lammer, H., Barabash, S., and Mousis, O.: Monte-Carlo simulation of Callisto's exosphere, *Icarus* 262, 14–29. <http://adsabs.harvard.edu/abs/2015Icar..262..14V>, 2015.

Wang, Y. C. and Ip, W. H.: Source dependency of exospheric sodium on Mercury. *Icarus* 216, 387–402. <http://dx.doi.org/10.1016/j.icarus.2011.09.023>, 2011.

10 Winslow, R. M., Johnson, C. L., Anderson, B. J., Korth, H., Slavin, J. A., Purucker, M. E., and Solomon, S. C.: Observations of Mercury's northern cusp region with MESSENGER's Magnetometer, *Geophys. Res. Lett.*, 39, L08112, doi:10.1029/2012GL051472, 2012.

Woodruff, D. P., Traum, M. M., Farrell, H. H., Smith, N. V., Johnson, P. D., King, D. A., Benbow, R. L., and Hurych, Z.: Photon- and electron-stimulated desorption from a metal surface, *Phys. Rev. B*, 21, issue 12, 5642–5645 doi:10.1103/PhysRevB.21.5642, 1980.

Wurz, P. and Lammer, H.: Monte-Carlo Simulation of Mercury's Exosphere, *Icarus* 164(1) 1–13. doi:10.1016/S0019-1035(03)00123-4,

15 2003.

Wurz, P., Rohner U., Whitby, J. A., Kolb, C., Lammer, H., Dobnikar P., and Martín-Fernández, J. A.: The Lunar Exosphere: The Sputtering Contribution, *Icarus* 191 486–496, doi:10.1016/j.icarus.2007.04.034, 2007.

Wurz, P., Whitby, J. A., Rohner U., Martín-Fernández, J. A., Lammer, H., and Kolb, C.: Self-consistent modeling of Mercury's exosphere by sputtering, micro-meteorite impact and photon-stimulated desorption, *Planet and Space Science* 58 1599–1616.

20 doi:10.1016/j.pss.2010.08.003, 2010.

Yakshinskiy, B. V. and Madey, T. E.: Photon-stimulated desorption as a substantial source of sodium in the lunar atmosphere, *Nature* 400, 642–644. doi: 10.1038/23204, 1999.

Yakshinskiy, B. V. and Madey, T. E.: Desorption induced by electronic transitions of Na from SiO₂: relevance to tenuous planetary atmospheres, *Surface Science*, Volume 451, Issue 1, Pages 160–165, ISSN 0039-6028, doi: 10.1016/S0039-6028(00)00022-4, 2000.

25 Yakshinskiy, B. V. and Madey, T. E.: Photon-stimulated desorption of Na from a lunar sample: temperature-dependent effects, *Icarus*, Volume 168, Issue 1, Pages 53–59, <http://dx.doi.org/10.1016/j.icarus.2003.12.007>, 2004.

Yakshinskiy, B. V. and Madey, T. E.: Temperature-dependent DIET of alkalis from SiO₂ films: Comparison with a lunar sample, *Surface Science*, Volume 593, Issues 1–3, 202–209, <https://doi.org/10.1016/j.susc.2005.06.062>, 2005.

Ziegler, J. F., Ziegler, M. D., and Biersack, J. P.: SRIM - The stopping and range of ions in matter, *Nuclear Instruments and Methods in*

30 *Physics Research B*, Volume 268, 1818 – 1823. doi: 10.1016/j.nimb.2010.02.091, 2010.